ACS NANO

www.acsnano.org

Article

Diagnostic-Mediated Interactive Superlattices Engineering for Threshold-Saltatory Visual Assessment of Tuberculous Meningitis

Zikang Chen, Jianli Lin, Yibo Zhao, Ying Sun, Ruomei Teng, Ming Li, Guoxu Zhao, Liang Chen, Caiping Ding,* and Youju Huang*

Cite This: *ACS Nano* 2026, 20, 5238–5249

Read Online

ACCESS | Metrics & More | Article Recommendations | Supporting Information

ABSTRACT: Nonlinear dynamic monitoring is crucial for assessing L-tryptophan (L-Trp) dysregulation progression in tuberculous meningitis (TBM); yet remains challenging due to conventional sensing probes' inherent nondirectionality and poor interfacial response control. Herein, we present a programmable organic-ligand-based self-assembly strategy to construct superlattice nanoprobes with structurally responsive, tunable interfaces. Precisely regulating ligand assembly integrates atomically dispersed platinum layers with organic ligand bilayers, forming an interactive nanobiosensing interface for real-time, quantitative detection of nonlinear L-Trp dynamics. The nanoplatform shows threshold-dependent colorimetric response: subtle monochromatic brightness shifts below 0.2 μM, and distinct multiphase color transitions via chromatic superposition above it, enabling visual discrimination of pathological L-Trp fluctuations in TBM. Integrated with machine learning-enhanced pattern recognition, it achieves robust self-calibration and zero false positives in complex clinical matrices. Compared to conventional methods (acid-fast staining, culture), it reduces processing time by >50%, boosts accuracy by >13%, and cuts reagent costs by >74%, establishing an effective paradigm for neuroinflammatory biomarker monitoring and enabling precise TBM diagnosis.

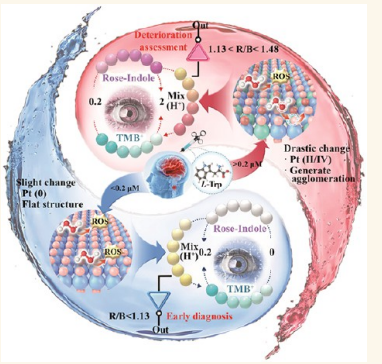

KEYWORDS: *interactive-superlattice, diagnostic-mediated, threshold-saltatory, visual biosensor, tuberculous meningitis*

INTRODUCTION

Traditional medical diagnostic methods focus on linear biomarker concentration changes. While these approaches are effective for conventional diseases, they prove insufficient for pathologies exhibiting nonlinear biomarker dynamics. Such pathologies include neurodegenerative diseases, autoimmune diseases, and other conditions with complex biomarker dynamics. Among these, tuberculous meningitis (TBM) represents a key diagnostic challenge. TBM induces meningeal inflammation and can lead to irreversible neurological deficits, representing one of the most severe clinical manifestations of tuberculosis.[1−3] Its subtle progression and nonspecific clinical manifestations complicate early diagnosis and severity assessment. The current gold-standard methods—cerebrospinal fluid (CSF) acid-fast staining and *Mycobacterium tuberculosis* culture—are constrained by low sensitivity, extended processing times, and an inability to evaluate disease progression.[4−6] Additionally, biomarkers such as adenosine dehydrogenase and acetylcholinesterase exhibit insufficient specificity for monitoring disease severity.[7] Therefore, there is an urgent need for tailored diagnostic tools capable of addressing both early detection and dynamic evaluation of TBM disease progression.

The metabolite L-tryptophan (L-Trp) has been identified as the most strikingly divergent compound in cerebrospinal fluid (CSF) during TBM analysis.[8,9] In early stage TBM, L-Trp concentrations sharply decline below 0.2 μM as part of a metabolic defense mechanism against inflammation.[10,11] As brain lesions worsen, L-Trp levels increase proportionally with the mortality risk, establishing 0.2 μM as a critical diagnostic and prognostic threshold. However, existing L-Trp detection technologies predominantly focus on enhancing chiral specificity and sensitivity while overlooking their dynamic role in disease progression. This oversight has resulted in a critical gap in real-time monitoring capabilities for clinical applications.[12,13] Notably, there are currently no probes or sensors capable of capturing threshold-specific signals or tracking nonlinear L-Trp fluctuations,[14] which are essential for advancing precision medicine in TBM.

To address this gap, interactive, stimulus-responsive nanomaterials have emerged as critical solutions. These advanced materials enable the translation of molecular-level information into macroscopic functional outputs in biological systems, which is achieved by leveraging their ability to adapt through structural reconfigurations triggered by environmental stimuli dynamically.[15−17] These systems exhibit programmable bio-

Received: December 3, 2025
Revised: January 24, 2026
Accepted: January 26, 2026
Published: February 6, 2026

https://doi.org/10.1021/acsnano.5c21167
ACS Nano 2026, 20, 5238−5249

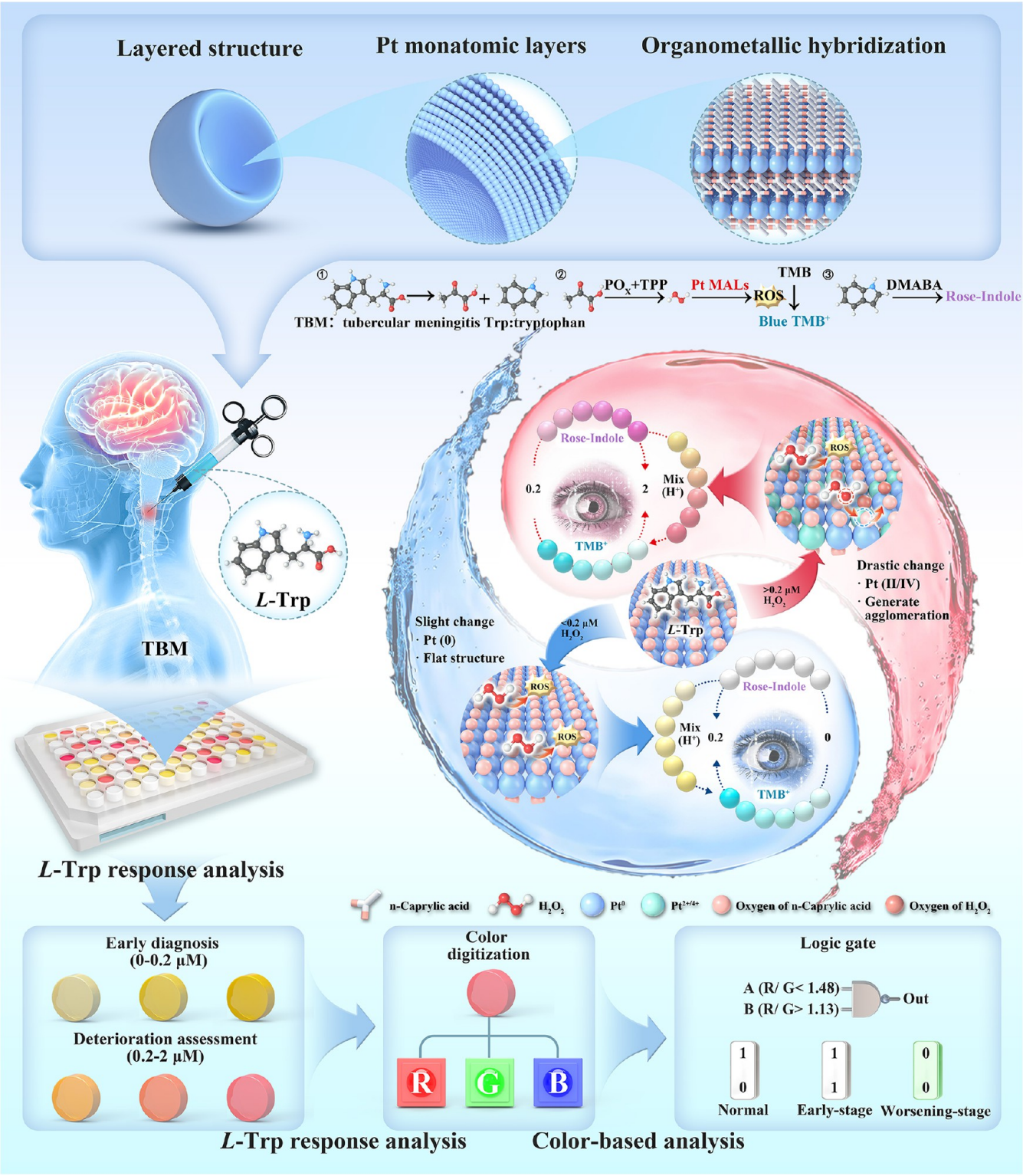

Figure 1. Schematic of a structure-mediated interactive differential visualization sensor array. Shown are the structure of Pt MALs, comprising an alternating arrangement of *n*-octanoic acid and platinum coordination centers; structural stability and color transition mechanism of Pt MALs in response to L-Trp; and logic-gate-based data analysis workflow for the accurate quantification of L-Trp concentration in cerebrospinal fluid (CSF) and accurate assessment of the disease progression.

sensor capabilities via modifiable geometric and electronic architectures, with layered material platforms serving as particularly prominent examples.[18,19] Among various feedback modes such as electrical, thermal, mechanical, and optical responses, the optical signals for color transitions offer distinct advantages in point-of-care diagnostics. These advantages include intrinsic quantifiability, operational simplicity, and compatibility with visual interpretation technologies that obviate the need for complex instrumentation.[20−22] This functional superiority establishes optical nanosensors as ideal

https://doi.org/10.1021/acsnano.5c21167
ACS Nano 2026, 20, 5238−5249

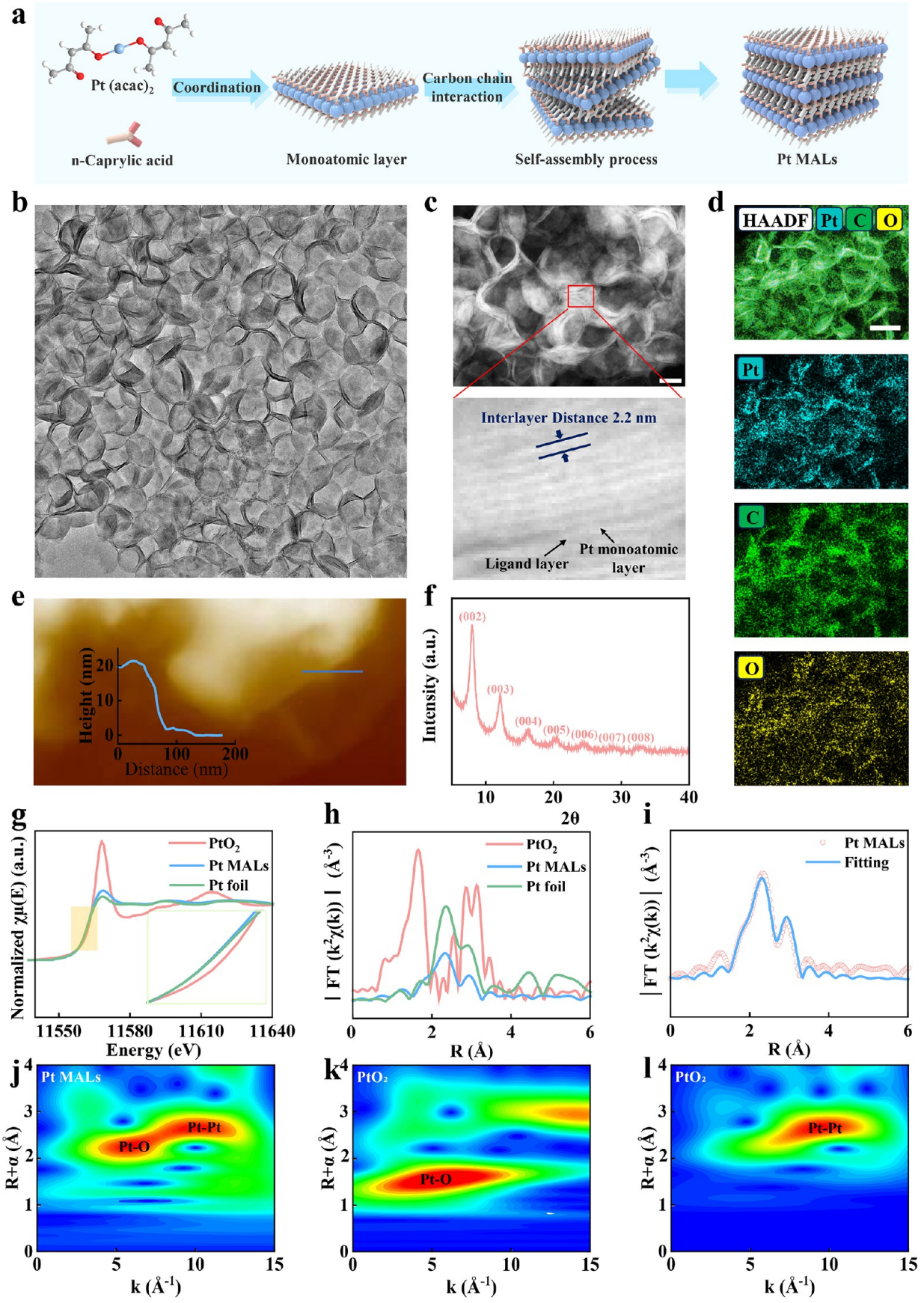

Figure 2. Synthesis and structural characterization of Pt MALs. (a) Schematic representation of the synthesis process of Pt MALs. (b) HR-TEM images; (c) HAADF-STEM images. (d) Energy-dispersive spectroscopy (EDS) images. (e) AFM images. (f) XRD patterns. (g) XANES spectra at

https://doi.org/10.1021/acsnano.5c21167
ACS Nano 2026, 20, 5238−5249

Figure 2. continued

Pt L3-edge. (h) k^2-weighted $\chi(k)$ function of the extended EXAFS spectra. (i) Comparison of theoretical and measured k^2-weighted $\chi(k)$ function of Pt MALs. (j–l) WT-EXAFS spectra of Pt MALs, PtO_2, and Pt foils (scales on all graphs represent 100 nm).

candidates for monitoring dynamic L-Trp distributions at a critical 0.2 μM threshold.

Therefore, the ideal visual sensor for monitoring the dynamic TBM marker L-Trp at the 0.2 μM threshold should exhibit the following attributes: (1) Reversible signal generation synchronized with L-Trp concentration fluctuations around the 0.2 μM transition point, ensuring precise threshold determination while minimizing observational subjectivity. (2) Sufficient sensitivity within the threshold range to enable real-time chromatic mapping of spatiotemporal L-Trp variations within ± 10% of the critical concentration. (3) Absolute specificity against interference from L-Trp regulatory components and metabolic intermediates, preserving monitoring fidelity. (4) Rapid-response architecture capable of cost-effective L-Trp analysis, with a processing speed 80% faster and a cost reduction of 60%, ensuring scalability in resource-constrained environments. These combined attributes facilitate dual functionality for both threshold confirmation and dynamic metabolic process tracking, representing an advancement beyond conventional binary detection paradigms.

In this study, Pt MALs were engineered through coordination bonds and van der Waals forces. These Pt MALs exhibit interactive peroxidase (POD)-like activity modulated by H_2O_2 concentrations (>0.20 μM) (Figure 1), enabling structural disintegration proportional to oxidative stress. By leveraging L-Trp's indole pathway, a dual-signal system was developed: (i) Indole reacted with 4-dimethylaminobenzaldehyde (DMABA) above 0.2 μM to form a pink product,[23,24] while (ii) pyruvate (a metabolite of L-Trp) triggers Pt MALs-mediated H_2O_2 generation, oxidizing TMB to produce a blue product. Below 0.2 μM, only the blue signal intensifies; above this threshold, the pink signal intensification coincides with blue attenuation due to the weakened POD-like activity. This inverse color interplay enhances the resolution for visual assessments. By integration of logic gates and RGB digitization, quantitative thresholds were established with 100% (for normal population) and 95.45% (for disease progression identification) accuracy, enabling simultaneous early diagnosis and deterioration monitoring. This next-generation diagnostic platform, which integrates nanocomposites, outperforms conventional TBM detection methods. It accelerates analytical processing by over 50%, boosts clinical sensitivity by over 13%, and reduces consumable costs by over 74% compared to acid-fast bacilli microscopy and mycobacterial culture. These improvements establish a tailored paradigm for real-time biomarker quantification in precision neurodiagnostic.

RESULTS AND DISCUSSION

Synthesis and Characterization of Pt MALs

A refined ligand regulation strategy was employed to synthesize self-assembled Pt MALs (Figure 2a). $Pt(acac)_2$ underwent reduction in n-caprylic acid solvent through CO generated from the thermal decomposition of $Mo(CO)_6$.[25,26] The *n*-octanoic acid-coordinated platinum species ($C_7H_{15}COOH$-Pt) was selected for comprehensive morphological characterization. High-resolution transmission electron microscopy (HR-TEM) and high-angle annular dark-field scanning transmission electron microscopy (HAADF-STEM) images revealed distinct lamellar superlattice structures featuring interconnected nanosheets with characteristic surface ridges and wrinkles. This phenomenon could be attributed to insufficient rigidity in the organic layer support (Figures 2b,c and S1). Structural characterization confirmed periodic Pt atomic layers separated by molecular ligands with an interlayer spacing of 2.20 nm and homogeneous Pt distribution (Figure 2d). The measured Pt MAL thickness (~0.4 nm) indicated a single-atomic-layer configuration, consistent with Pt's atomic radius (1.83 Å). Atomic force microscopy (AFM) measurements verified an average nanosheet thickness of 20.0 nm (Figure 2e). X-ray diffraction (XRD) and X-ray absorption fine structure (XAFS) analyses (Figures 2f–l and S2–S3) exhibited exclusive (00*l*)-series diffraction patterns corresponding to the 2.20 nm periodicity, indicative of highly ordered layered organization resembling organic 2D superlattices and organic–inorganic perovskite alternating structures.[27–30]

The material exhibited significantly enhanced peak intensity in the X-ray absorption near-edge structure (XANES) spectra compared with Pt foils, indicating electron-deficient characteristics. Extended edge X-ray absorption structure (EXAFS) analysis further confirmed the coexistence of Pt–Pt and Pt–O bonds (Figures 2i,j and S3), with Pt–Pt bond lengths averaging 3.11 Å, notably longer than the 2.79 Å observed in Pt foil (Table S1).

A markedly reduced Pt–Pt scattering intensity was observed in the first coordination shell, accompanied by a coordination number (CN) of approximately 6.2. This CN value deviated substantially from both the closely packed Pt foil structure and ideal monatomic layers, suggesting a low-ordered amorphous configuration.[31] Wavelet-transform analysis of XAFS data, visualized through color contour maps, facilitated precise bond length determination and intuitive atom-type identification. Distinct Pt–O and Pt–Pt signal peaks in Figure 2k–l display chromatic divergence from reference standards, thereby displaying the structural conclusions.

Feasibility Analysis of Structure-Mediated Self-Responsive Pt MALs and Its Catalytic Mechanism

Due to the highly ordered structure of Pt MALs and the exceptional catalytic performance exhibited by Pt nanomaterials, an extraordinarily sensitive response of Pt MALs toward H_2O_2 was observed at concentrations as low as 0–0.2 μM, accompanied by the formation of TMB oxide (Figure S4). A strong linear relationship existed between H_2O_2 concentration and TMB absorbance (y = 10.9484 x + 0.0919, R^2 = 0.998), although this linearity diminished at higher concentrations (Figure S5). Elucidating the distinct POD-like activity mechanism of Pt MALs is crucial for understanding the rationality of the catalytic reaction under varying H_2O_2 concentrations.

First, to investigate the origin of the POD-like activity in Pt MALs', we systematically probed three reactive oxygen species (ROS) through selective scavenging approaches. Specific scavengers—*p*-benzoquinone (PBQ) for superoxide radical ($O_2^{\bullet-}$), 1, 3-diphenylisobenzofuran (DPBF) for singlet oxygen

https://doi.org/10.1021/acsnano.5c21167
ACS Nano 2026, 20, 5238–5249

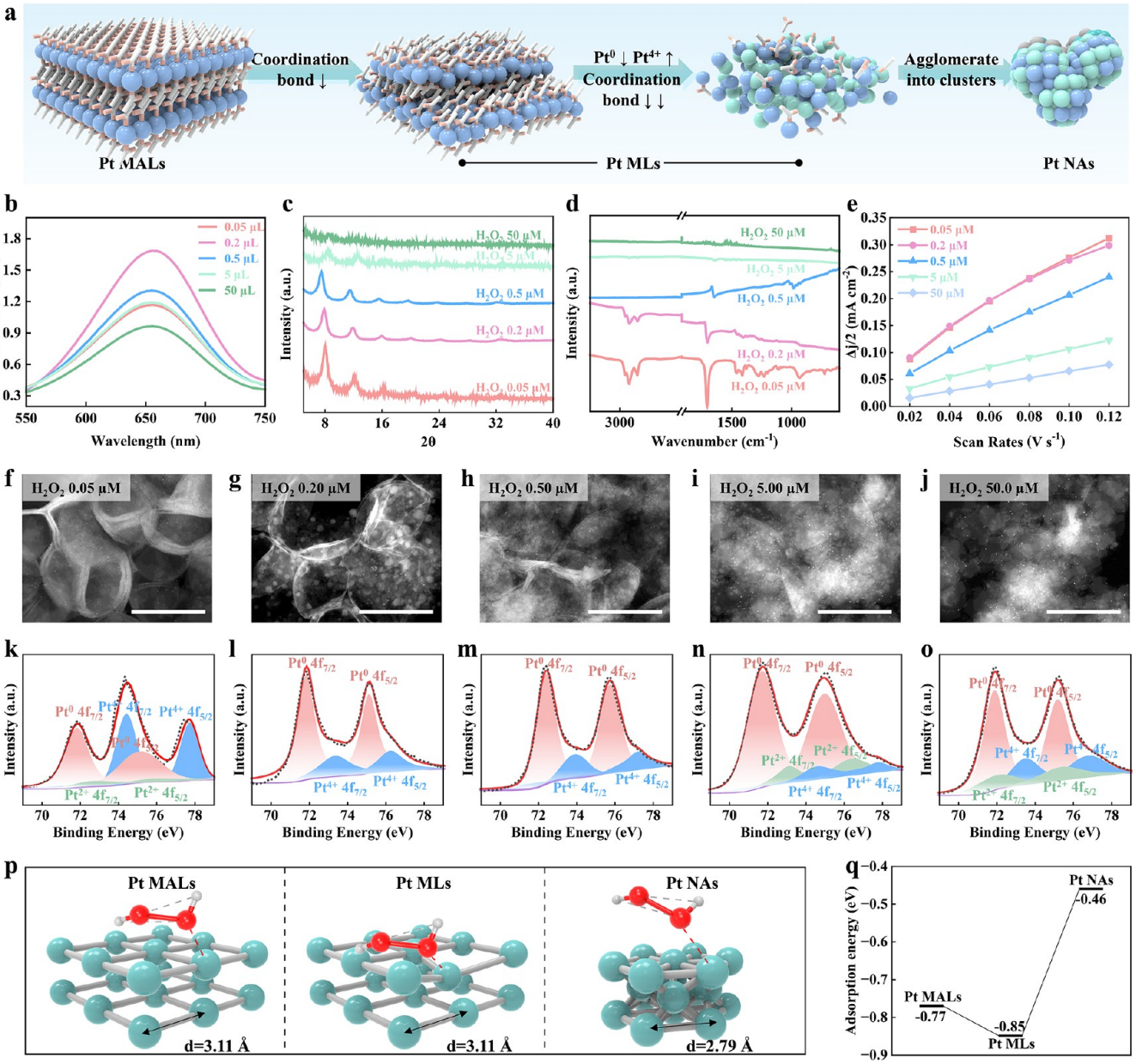

Figure 3. Verification of the interactive performance of Pt MALs. (a) Schematic representation of the mechanism by which H_2O_2 induces the structural changes in Pt MALs. Under the influence of different concentrations of H_2O_2. (b) Absorbance spectra of TMB catalyzed by Pt MALs. (c) FTIR spectra, (d) XRD patterns. (e) ESS dot plot. (f–j) TEM images and (k–o) XPS spectra were acquired. (p) In the three stages of Pt MALs, Pt MLs, and Pt NAs, the simulation of the adsorption process of H_2O_2 and (q) changes in the binding energy of Pt MALs, Pt MLs, and Pt NAs.

($^1O_2$), and terephthalic acid (TA) for hydroxyl radical ($^\bullet$OH)—were employed.[32−34] Experimental results demonstrated that under Pt MALs catalysis, PBQ and DPBF effectively captured their corresponding ROS, generating characteristic spectral signals (Figures S6a and S7a), while TA exhibited fluorescence upon interaction with $^\bullet$OH (Figure S8a). For enhanced validation, electron paramagnetic resonance (EPR) coupled with spin-trapping techniques was implemented: 5,5-dimethyl-1-pyrroline-*N*-oxide (DMPO) served as the probe for $O_2^{\bullet-}$/$^\bullet$OH, and 2,2,6,6-tetramethylpiperidine-*N*-oxygen (TEMPO) for $^1O_2$.[35,36] EPR analysis revealed that in the presence of Pt MALs and H_2O_2, the $O_2^{\bullet-}$ specific spectrum displayed a 1:1:1:1 quartet pattern (Figure S6b), whereas no significant signal emerged in the Pt MALs-only systems. Distinct spectral signatures for $^1O_2$ (1:1:1 triplet) and $^\bullet$OH (1:2:2:1 quartet) were also identified (Figures S7b and S8b). These findings indicated that the POD-like activity of Pt MALs originates from their catalytic capacity to oxidize H_2O_2 into three ROS species: $O_2^{\bullet-}$, $^1O_2$, and $^\bullet$OH.

Second, we systematically investigated the structural evolution of Pt MALs under varying H_2O_2 concentrations. As shown in Figure 3a, three distinct structural stages were identified: intact monatomic layers (Pt MALs), granular layers (Pt GLs) characterized by partial bond rupture and oxidation, and nanoagglomeration (Pt NAs) marked by severe aggregation and oxidation. At lower concentrations of H_2O_2 (<0.2 μM), ROS was generated by partial H_2O_2 decomposition. The excess H_2O_2 and intermediates occupied catalytic sites, attacking Pt atoms by coordination with *n*-

https://doi.org/10.1021/acsnano.5c21167
ACS Nano 2026, 20, 5238−5249

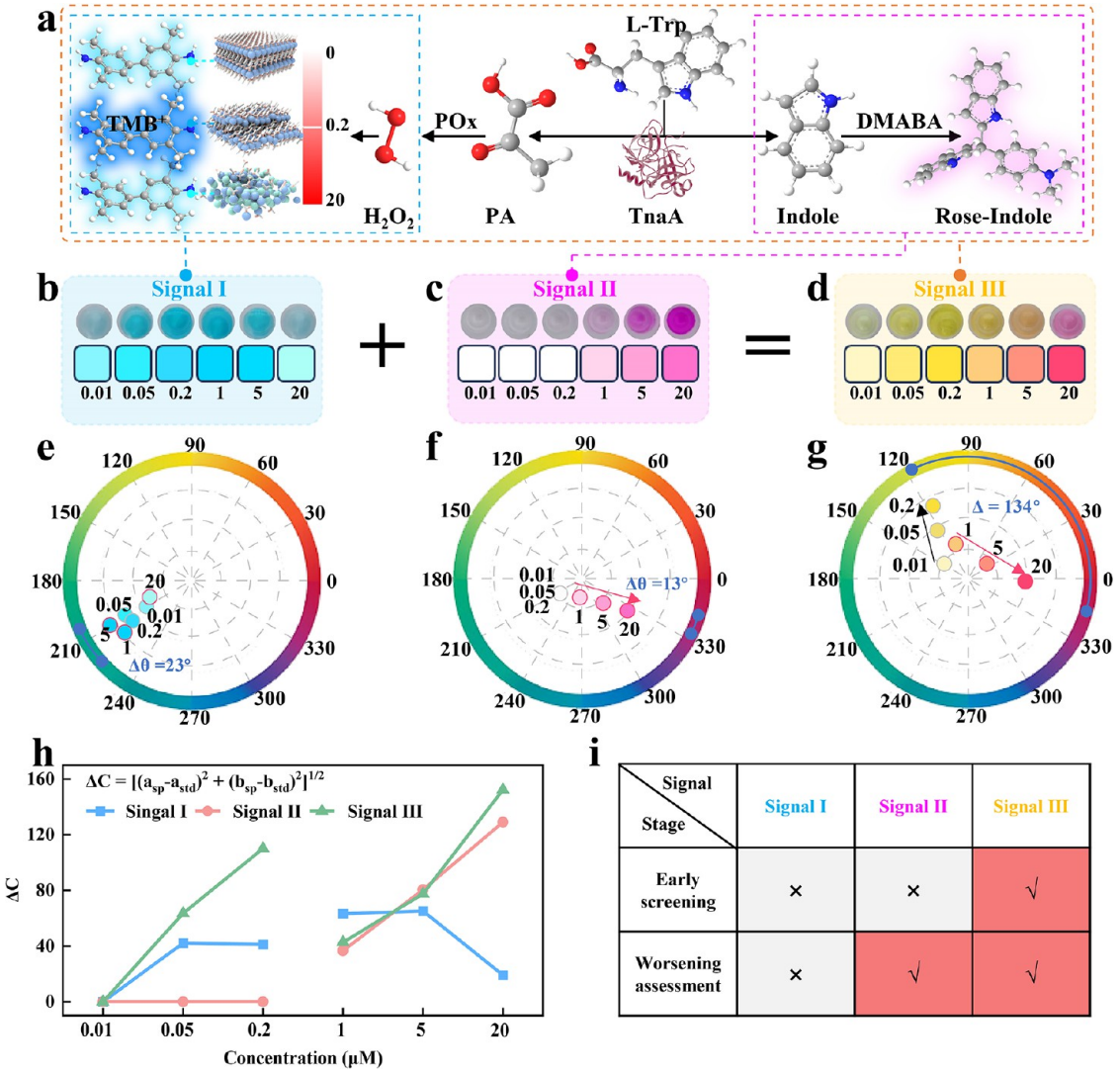

Figure 4. Feasibility verification of monochrome and multicolor color development. (a) Schematic illustration of the color development mechanism. (b–d) Color relationship diagrams for the blue, pink, and composite color pathways. (e–g) CIE chromaticity diagrams corresponding to the three color pathways. (h) Variation in ΔC as a function of H_2O_2 concentration shown by three distinct curves. (i) Potential of the three color pathways to discriminate between patients in early and advanced stages of TBM.

octanoic acid. The disrupted coordination bonds collapse the layered structure into nanoclusters or nanoparticles. The loss of coordination further exposed Pt atoms to the oxidation state, resulting in electron-deficient $Pt^{2+/4+}$ states.

This mechanism was further confirmed by an additional analysis. The TMB^+ absorption peak at 652 nm (Figure 3b) initially rises but subsequently declines beyond 0.2 μM H_2O_2, indicating structural damage and diminished POD-like activity. Fourier-transform infrared spectroscopy (FTIR) revealed a weakening C=O stretching vibration at 1640 cm^{-1} with increasing H_2O_2 levels (Figure 3c), consistent with carboxylic acid dissociation and structural destabilization.[37,38] XRD patterns further demonstrated a progressive weakening of the (00*l*) diffraction signals, nearly disappearing at 5 μM H_2O_2 (Figure 3d). Electrochemical assessments via cyclic voltammetry (Figures 3e and S9) revealed a stable catalytic performance below 0.2 μM H_2O_2 but a sharp decline above this threshold, aligning with structural collapse and alteration of active sites.

TEM imaging (Figures 3f-j and S10) visualized progressive agglomeration. At 0.2–5.0 μM H_2O_2, Pt MALs lost structural integrity, forming nanoparticles by 50 μM H_2O_2. XPS analysis (Figure 3k–o) further confirmed the initial coexistence of Pt^0 and Pt^{4+} states.[39] Increasing H_2O_2 reduced Pt^{4+} peaks (due to coordination bond rupture), while Pt^{2+} emerged at >5 μM H_2O_2, reflecting the oxidation of unprotected Pt atoms. Notably, valence shifts did not strictly correlate with the POD-like activity inflection points.

Density functional theory (DFT) calculations further elucidated the adsorption energy trends: Pt MLs exhibited maximal binding energy (hindering H_2O_2/product desorption), Pt NAs showed minimal energy (promoting premature desorption), and Pt MALs balanced these extremes (Figures 3p–q and S11). Excessive H_2O_2 (>0.2 μM) saturated catalytic sites (Figure S12), disrupting adsorption–desorption equilibrium and inducing catalyst poisoning. Collectively, these findings established Pt MALs as adaptive catalysts responsive to H_2O_2 gradients with 0.2 μM serving as a critical stability threshold.

https://doi.org/10.1021/acsnano.5c21167
ACS Nano 2026, 20, 5238–5249

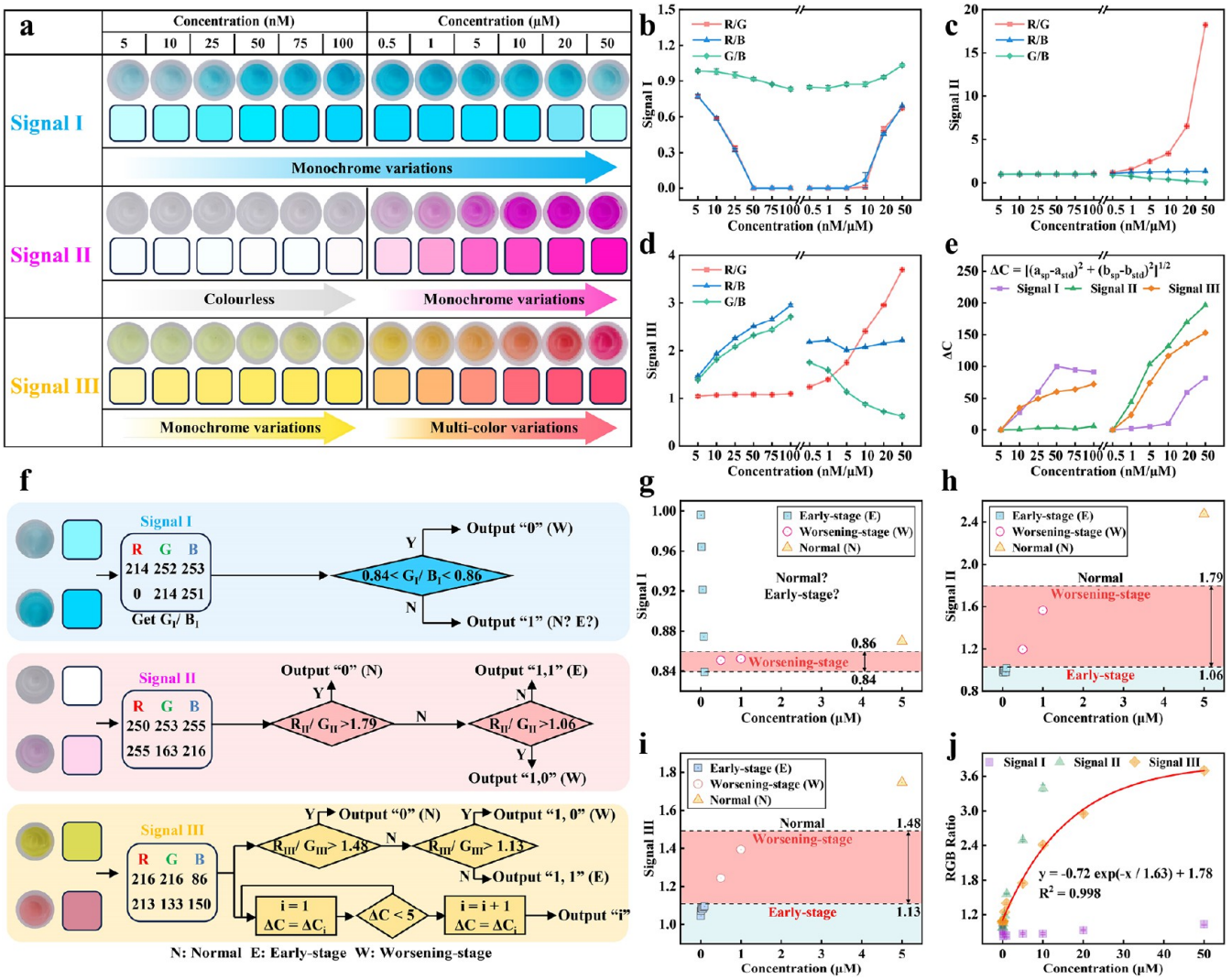

Figure 5. Design logic gate to realize TBM disease diagnosed. (a) Color signal response patterns corresponding to different concentrations of L-Trp. (b–d) Variations in the RGB digital signal ratios for the three color pathways as a function of H_2O_2 concentration (n = 3). (e) The ΔC change curves of the three color pathways. (f) Schematic diagram of the logic gate design based on the three chromatic signals. (g–i) Discrimination results generated by the logic gate operations (blue square markers: Early stage; red dot markers: Worsening-stage; yellow square markers: Normal). (j) Statistical fitting analysis of the correlation between L-Trp concentration and the colorimetric signals (n = 3).

Feasibility Verification Differentiated Visualization Sensor-Based Self-Responsive Pt MALs

To advance early diagnosis and deterioration assessment of TBM, researchers identified L-Trp as a critical biomarker through its metabolic pathway involving pyruvate and indole. Pyruvate metabolism generated H_2O_2 via enzymatic cascades, while Pt MALs exhibited self-responsive behavior to H_2O_2 concentrations with 0.2 μM serving as a threshold. This system enabled colorimetric detection of L-Trp levels (<0.2 μM) through the oxidation of TMB to blue TMB^+. However, reliance on monochromatic signals (e.g., blue intensity) introduced limitations in resolution and susceptibility to errors. To address this, we exploited a secondary pathway: indole, a cometabolite of L-Trp, formed a pink rose-indole complex with DMABA at concentrations >0.2 μM. By integrating Pt MALs' H_2O_2-responsive monochromatic signals with indole-DMABA multicolor outputs, we developed a dual-pathway visual sensor with enhanced discriminative power (Figure 4a).

The first pathway employed pyruvate oxidase (POx) and Pt MALs to catalyze pyruvate into ROS, which oxidized TMB to blue TMB^+. Pt MALs' feedback modulation of H_2O_2 induced nonlinear brightness shifts: color intensified at <0.2 μM H_2O_2 and attenuated at >0.2 μM (Figure 4b). The second pathway leveraged the complexation of indole with DMABA, yielding a pink signal that is detectable exclusively at indole concentrations of ≥0.2 μM (Figure 4c). Synergistic integration of these pathways yielded distinct colorimetric profiles: a singular yellow hue at 0–0.2 μM and a multicolor gradient (yellow → orange → pink) at 0.2–20 μM (Figure 4d). Composite color transitions (wide range of 134°) exhibited superior visual discriminability compared to monochromatic shifts (23° for blue; 13° for pink), as quantified by CIE chromaticity analysis (Figure 4e–g). Notably, composite color trajectories aligned orthogonally to monochromatic brightness trends (radiating from the white light source), which capitalize on the higher sensitivity of the human visual system to chromatic diversity than to luminance variation.

https://doi.org/10.1021/acsnano.5c21167
ACS Nano 2026, 20, 5238–5249

Theoretical chromo simulations confirmed the self-regulating behavior of Pt MALs. At H_2O_2 concentrations >0.2 μM (Mode A), blue signal attenuation coincided with pink intensification; conversely, at H_2O_2 concentrations <0.2 μM (Mode B), the blue signal is enhanced while latent pink formation occurs (Figures S13−S14). Blending studies (Figure S15) demonstrated that the superposition of Mode A generates brighter and spectrally broader outputs (higher RGB values) compared to the monochromatic bias of Mode B's. These findings validated Pt MALs' capacity for adaptive signal modulation between monochrome and polychrome states, thereby enhancing diagnostic resolution.

Digital colorimetric analysis (Figure 4h,i) further validated the system's quantitative utility. After image capture under controlled studio conditions and uniform color processing, ambient light interference was effectively minimized. The color difference was then quantified using the ΔC metric. The calculation is as follows:

$$a = 500[(0.41R + 0.36G + 0.18B) - (0.21R + 0.72G + 0.07B)] \quad (1)$$

$$b = 200[(0.21R + 0.72G + 0.07B) - (0.21R + 0.72G + 0.07B)] \quad (2)$$

$$\Delta C = [(a_{sp} - a_{std})^2 + (b_{sp} - b_{std})^2]^{1/2} \quad (3)$$

where a and b are two coordinate values in the CIELab color space.

The results revealed that the ΔC of the blue pathway exhibited a nonmonotonic pattern, whereas the effective dynamic range of the pink pathway was limited to the high-concentration region. In contrast, the composite color pathway showed a consistent positive correlation across both low and high concentration gradients, thereby enhancing the interpretability of the results. This tripartite differentiation highlighted the limitations of single-color diagnostics and underscored the critical importance of multiplexed detection for an accurate TBM progression assessment. Collectively, this H_2O_2-interactive Pt MALs platform demonstrated substantial potential for advancing point-of-care TBM evaluation through dual-pathway chromatic discrimination.

The Differentiated Visualization Sensor for Highly Sensitive Detection of L-Trp

To achieve optimal enzyme activity and experimental efficacy, a precisely optimized catalytic pH and reaction time was used for TnaA, POx, and Pt MALs. As shown in Figure S16, all enzymes demonstrated peak performance under weakly acidic conditions. TnaA and POx exhibited maximal TMB-mediated chromogenic responses at pH 6.5 and 6.7, respectively, while Pt MALs required a more acidic environment (pH 5.5). Temporal optimization revealed divergent kinetics: TnaA and POx required 60 min of incubation for optimal catalysis, while Pt MALs achieved maximum substrate conversion within 20 min, indicating superior catalytic efficiency. The system's selectivity was also rigorously evaluated through interference studies (Figure S17) involving physiologically relevant compounds, including 10 amino acids and 9 pyruvate structural analogs/metabolites. Notably, neither L-Trp nor pyruvate detection exhibited significant signal perturbation (variation <5%), confirming exceptional specificity despite complex matrix conditions. Furthermore, Pt MALs exhibit excellent structural stability, maintaining their structural integrity under conditions involving complex matrices, physiologically relevant pH values, and wide temperature fluctuations (Figures S18−S19).

Quantitative analysis established two distinct detection regimes (Figure 5a). In the ultrasensitive range (0.005−0.2 μM), a linear correlation ($\Delta\lambda_{max}$ = 10.94c + 0.09, R^2 = 0.998) between TMB^+ absorbance and L-Trp concentration was observed (Figure S20a,b). This regime further leverages TMB^+ to TMB^{2+} acidification, yielding yellow signals optimized for nanomolar detection through human ocular sensitivity to blue-spectrum signals. At elevated concentrations (0.2−50 μM), dual signal transduction emerged: while H_2O_2-mediated Pt MALs inhibition reduced catalytic linearity ($\Delta\lambda_{max}$ = 0.9 + 0.39 lg(c), R^2 = 0.988), indole-derived rose-red chromogenesis demonstrated robust concentration dependence ($\Delta\lambda_{max}$ = 0.03c + 0.28, R^2 = 0.999) through distinct extinction peaks (Figure S20c−f). Spectral deconvolution confirmed minimal TMB^{2+} interference ($\Delta\lambda_{max}$ = 0.10 + 0.02c, R^2 = 0.998), enabling accurate colorimetric differentiation from orange to red hues.

Comparative chromatic analysis (Figure S21) revealed significantly enhanced visual discrimination through composite coloration compared with monochromatic TMB^{2+} signals, with chromatic angle variations ($\Delta\theta$ = 103° vs 26°) demonstrating superior human perceptibility. This dual-mode detection system achieved unprecedented sensitivity (0.005 μM) and a dynamic range spanning 4 orders of magnitude, outperforming existing L-Trp assays (Figure S22). The Pt MALs-mediated self-responsive platform not only enabled ultratrace detection but also provided intuitive colorimetric outputs across clinically relevant concentration ranges, establishing a robust and versatile methodology for TBM diagnostics and disease progression monitoring.

Design of Logic Gate Assisted Differentiated Visualization Sensor to Accurately Assess TBM Disease Progression

To obtain more robust quantitative data, RGB values were digitally extracted from the monochromatic (blue and pink) and composite color signals (Figures 5a and S23), followed by ratio calculations (Figures 5b−d). The analysis revealed that the R/G and R/B ratios of the blue signal exhibited negligible responsiveness (approaching zero) across a wide concentration range, thereby limiting its diagnostic utility. As a result, the G/B ratio was the only viable option for this pathway. The pink signal, although colorless and thus ineffective for detection at low concentrations, exhibited its greatest dynamic range in the R/G ratio at high concentrations. Similarly, the composite color signal also displayed the largest dynamic range in its R/G ratio with a distinct advantage: it provided effective response coverage across the entire concentration range. Subsequent ΔC value calculations (Figure 5e) further confirmed the superiority of the composite signal. Considering both the dynamic range of the ΔC and its linear correlation, the composite color signal demonstrated a clear and significant advantage for quantitative identification.

Within the logic gate architecture (Figure 5f), the key operational parameters are the G/B ratio (from the blue pathway), the R/G ratio (from the pink pathway), and the R/G ratio (from the composite color pathway). For the blue signal-based gate, a "Yes" output of "0", indicative of the deteriorated stage of meningitis, is activated when the G/B value falls within the threshold of 0.84 to 0.86 (Figure 5g).

https://doi.org/10.1021/acsnano.5c21167
ACS Nano 2026, 20, 5238−5249

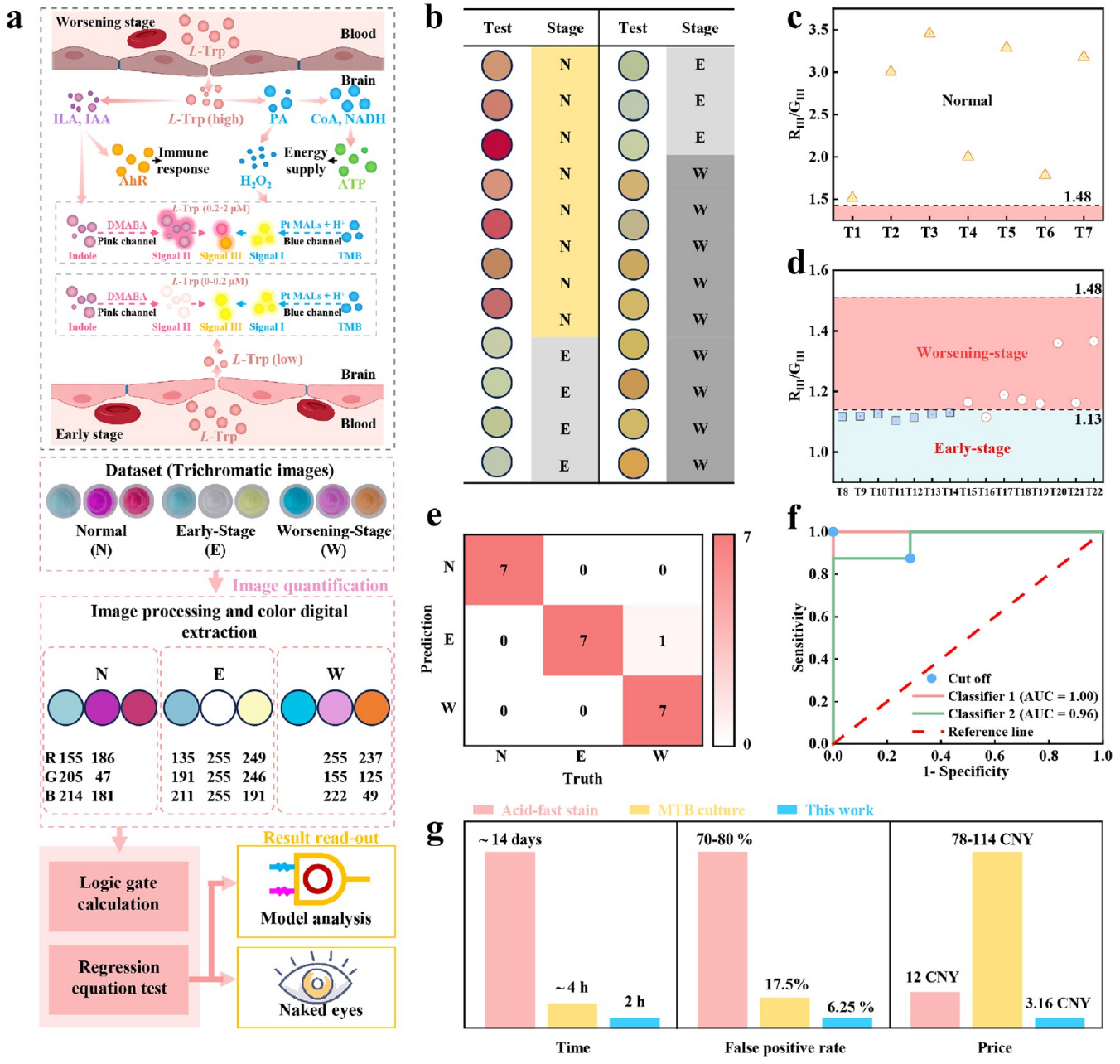

Figure 6. Screen TBM patients in combination with logic gates. (a) Schematic representation of the physiological role of L-Trp and the colorimetric visualization-based workflow for patient screening. (b) Representative color palette and (c, d) corresponding scatter plots for the diagnosis of clinical samples using the composite color logic gate. (e) Evaluation of the logic gate's diagnostic performance using a confusion matrix and (f) ROC curve analysis. (g) Comparison of the time requirement, false positive rate, and cost between the present method and two established gold-standard diagnostic techniques.

Values outside this range prevent reliable differentiation between patients and healthy individuals. The logic gate for the pink signal employs a two-step recognition process: an R/G value greater than 1.79 yields an output of "0" (signifying a normal subject). For values below 1.79, a second determination distinguishes early stage TBM patients (R/G < 1.06) from those in the deteriorated stage (R/G between 1.06 and 1.79) (Figure 5h). The composite color signal-based gate follows a similar two-step logic, with thresholds set at >1.48 (normal), 1.13−1.48 (deteriorated stage), and <1.13 (early stage) (Figure 5i). To enhance diagnostic reliability for large-scale screening, all outputs were subjected to rigorous secondary validation against a standard curve (Figure 5j), which also enables simultaneous reporting of the corresponding L-Trp concentration. This quantitative capability represented a distinct advantage of the composite signal, as the data from the two single-color pathways lack sufficient correlation for a reliable curve fitting with a high R^2 value.

The implemented logic operations enabled advanced image data inference through digital signal conversion, effectively distinguishing dual-input responses from single inputs or noise inputs. This computational approach facilitated both early TBM detection and accurate deterioration assessment by leveraging three critical capabilities: (1) threshold-based pathological classification, (2) quantitative progression tracking via chromatic phase transitions, and (3) noise-resistant

https://doi.org/10.1021/acsnano.5c21167
ACS Nano 2026, 20, 5238−5249

signal discrimination through combinatorial logic. This methodology demonstrated substantial potential for optimizing diagnostic specificity in resource-constrained settings while maintaining analytical rigor comparable to that of conventional laboratory techniques.

Logic Gate Assisted Differentiated Visualization Sensor to Screening TBM Patients

Building upon robust laboratory findings, we validated our detection system using authentic cerebrospinal fluid (CSF) samples stratified by L-Trp concentration (high, medium, low). Prior to analysis, a calibration curve was established by using a commercially available L-Trp quantification kit (Figure S24). Subsequently, cerebrospinal fluid samples were analyzed using our platform through colorimetric detection with the resulting signals interpreted by the predefined logic gate method (Figure 6a; original data in Table S2). The test results for the 22 clinical samples are presented in Figure 6b, and detailed identification criteria were illustrated in Figure 6c,d. In the primary classification step, all early stage patients were accurately identified, with the R/G ratios of all normal samples exceeding the threshold of 1.48. During the secondary classification, early stage samples were accurately distinguished once again; however, one sample from the deteriorated stage was misclassified, likely due to an excessively strong host immune response. Classification performance, evaluated using a confusion matrix, achieved accuracies of 100 and 93% in the first and second steps, respectively (Figure 6e). Receiver Operating Characteristic (ROC) analysis further confirmed the clinical utility of the method. The first classification step achieved perfect performance with specificity at 100%, supported by an AUC of 1.00. The second step maintained a high diagnostic standard, exhibiting a specificity of 100%, and an AUC of 0.96 (Figure 6f).

A comparative assessment against standard TBM diagnostic modalities (acid-fast smear and *Mycobacterium tuberculosis* culture) revealed critical advantages: the platform achieved superior diagnostic speed (>50% reduction in processing time), enhanced accuracy (>13% improvement in detection rate), and significant cost-efficiency (>74% reduction in reagent expenses) (Figure 6g). These findings collectively demonstrated the technical superiority and clinical applicability of our system, particularly through its synergistic combination of colorimetric analysis and logic operations, which effectively addressed the inherent sensitivity-specificity trade-off in conventional CSF diagnostics.

CONCLUSION

In this study, we engineered a structure-mediated leap-type interactive visualization biosensor for the ultrasensitive detection of L-Trp, which facilitates both early diagnosis and progression assessment of TBM. The Pt MALs probe demonstrated robust catalytic activity, producing a distinct signal at the diagnostic threshold for L-Trp. This multistage colorimetric transition enhanced the biosensor's ability to differentiate between positive cases and severe deterioration states. Compared with conventional single-mode detection systems and clinical colorimetric assays, our leap-type interactive design amplified the variation in signals across negative, positive, and severe stages. This significantly improved the diagnostic accuracy for both early TBM identification and deterioration monitoring. Furthermore, the integration of logic-gate functionality allowed for precise quantitative analysis of L-Trp in complex biological matrices. A comparative analysis with standard TBM diagnostics revealed marked improvements: our platform achieved an over 50% reduction in processing time, an over 13% increase in detection accuracy, and an over 74% reduction in reagent costs. These advancements position this diagnostic platform as a solution to long-standing clinical challenges in TBM detection by simultaneously enhancing speed, precision, and cost-efficiency relative to conventional gold-standard methods. In the future, the structure-mediated leap-type interactive visual biosensor has the potential to expand the detection of immune system biomarkers associated with other infectious neurological diseases, such as encephalitis and myelitis, and could facilitate the development of rapid and accurate diagnostic platforms for these conditions.

EXPERIMENTAL SECTION

Synthesis of Pt MALs

The $Pt(acac)_2$ (20 mg) was dissolved in n-caprylic acid (16 mL) at room temperature, and oxygen was purged with argon gas. Subsequently, $Mo(CO)_6$ (30 mg) was added to the mixture, and the mixture was stirred continuously for 30 min. The resulting solution was transferred to an oil bath and heated at 90 °C for 2 h, followed by centrifugation to collect the precipitate, which was then washed with a solution of *n*-hexane and ethanol.

L-Trp Detection

In the PBs buffer system, a solution of TnaA and various concentrations of substrate L-Trp were combined to obtain a 200 μL mixed solution, which was then incubated at 37 °C for 60 min. From this mixed solution, Mixed Solution 1 was extracted and treated with DMABA solution and hydrochloric acid solution to adjust the total volume to 200 μL, resulting in a rose red solution through a complexation reaction. The absorption spectrum was measured using an ultraviolet spectrophotometer, and the color results were observed and recorded. Another equal amount of Mixed Solution 1 was taken and supplemented with POx solution (20 U/L), TPP solution (10 mM), and $MgCl_2$ solution (1 mM) to reach a total volume of 220 μL. After incubating at 37 °C for 60 min, Pt MALs (20 μL) and TMB solution were added for further incubation, resulting in Product 2 Solution through reoxidation reaction. The absorption spectrum was measured again, and the color results were recorded. Finally, the Product 1 Solution and Product 2 Solution were mixed in equal amounts before the final results.

Testing of Real Samples

The cerebrospinal fluid and serum from mice were extracted using standard procedures and thoroughly mixed with TnaA in a PBs buffering system. No changes were made to the remaining steps. Finally, the experimental results were recorded and compared to the standard curves of commercial kits for calculating the RSD and recovery rate.

ASSOCIATED CONTENT

Data Availability Statement

The data that support the findings of this study are available in the Supporting Information of this article.

https://doi.org/10.1021/acsnano.5c21167
ACS Nano 2026, 20, 5238−5249

Supporting Information

The Supporting Information is available free of charge at https://pubs.acs.org/doi/10.1021/acsnano.5c21167.

The chemicals used; characterization instruments and means; the catalytic mechanism and parameters of Pt MALs were optimized, the absorbance spectra and linear graphs of L-Trp were detected, and the detection performance was compared with that of cerebrospinal fluid reported in the literature (PDF)

AUTHOR INFORMATION

Corresponding Authors

Caiping Ding − *College of Life and Environmental Sciences; College of Material Chemistry and Chemical Engineering; and the Affiliated Hospital of Hangzhou Normal University, Hangzhou Normal University, Hangzhou, Zhejiang 311121, China;* orcid.org/0000-0002-2066-3392; Email: cpding@hznu.edu.cn

Youju Huang − *College of Life and Environmental Sciences; College of Material Chemistry and Chemical Engineering; and the Affiliated Hospital of Hangzhou Normal University, Hangzhou Normal University, Hangzhou, Zhejiang 311121, China;* orcid.org/0000-0001-5815-9784; Email: yjhuang@hznu.edu.cn

Authors

Zikang Chen − *College of Life and Environmental Sciences; College of Material Chemistry and Chemical Engineering; and the Affiliated Hospital of Hangzhou Normal University, Hangzhou Normal University, Hangzhou, Zhejiang 311121, China*

Jianli Lin − *College of Life and Environmental Sciences; College of Material Chemistry and Chemical Engineering; and the Affiliated Hospital of Hangzhou Normal University, Hangzhou Normal University, Hangzhou, Zhejiang 311121, China*

Yibo Zhao − *College of Life and Environmental Sciences; College of Material Chemistry and Chemical Engineering; and the Affiliated Hospital of Hangzhou Normal University, Hangzhou Normal University, Hangzhou, Zhejiang 311121, China*

Ying Sun − *College of Life and Environmental Sciences; College of Material Chemistry and Chemical Engineering; and the Affiliated Hospital of Hangzhou Normal University, Hangzhou Normal University, Hangzhou, Zhejiang 311121, China*

Ruomei Teng − *College of Life and Environmental Sciences; College of Material Chemistry and Chemical Engineering; and the Affiliated Hospital of Hangzhou Normal University, Hangzhou Normal University, Hangzhou, Zhejiang 311121, China*

Ming Li − *College of Life and Environmental Sciences; College of Material Chemistry and Chemical Engineering; and the Affiliated Hospital of Hangzhou Normal University, Hangzhou Normal University, Hangzhou, Zhejiang 311121, China*

Guoxu Zhao − *College of Life and Environmental Sciences; College of Material Chemistry and Chemical Engineering; and the Affiliated Hospital of Hangzhou Normal University, Hangzhou Normal University, Hangzhou, Zhejiang 311121, China*

Liang Chen − *College of Life and Environmental Sciences; College of Material Chemistry and Chemical Engineering; and the Affiliated Hospital of Hangzhou Normal University, Hangzhou Normal University, Hangzhou, Zhejiang 311121, China*

Complete contact information is available at: https://pubs.acs.org/10.1021/acsnano.5c21167

Notes

The authors declare no competing financial interest.

ACKNOWLEDGMENTS

This work was financially supported in part by the "Pioneer" and "Leading Goose" R&D Program of Zhejiang (2024C03195), the National Natural Science Foundation of China (U25A20385), the "Pioneer" and "Leading Goose" R&D Program of Zhejiang (2025C02250(SD2)), the Interdisciplinary Research Project of Hangzhou Normal University (2024JCXK01), and the Zhejiang Provincial Natural Science Foundation of China (LMS26B050007).

REFERENCES

(1) Huynh, J.; Donovan, J.; Phu, N. H.; Nghia, H. D. T.; Thuong, N. T. T.; Thwaites, G. E. Tuberculous meningitis: progress and remaining questions. *Lancet Neurol.* **2022**, *21*, 450−464.

(2) Dong, C.; Huang, C. Y.; Q, X.; Cheng, H.; Zheng, D. W.; Hong, S.; Yan, Y.; Niu, M. T.; Xu, J. G.; Zhang, X. Z. Neisseria meningitidis Opca protein/MnO_2 hybrid nanoparticles for overcoming the blood-brain barrier to treat glioblastoma. *Adv. Mater.* **2022**, *34*, No. e2109213.

(3) Wasserman, S.; Harrison, T. S. Tuberculous meningitis - new approaches needed. *N. Engl. J. Med.* **2023**, *389*, 1425−1426.

(4) Davis, A. G.; Wilkinson, R. J. Diagnostic tests for tuberculous meningitis. *Lancet Infect. Dis.* **2020**, *20*, 262−263.

(5) Donovan, J.; Figaji, A.; Imran, D.; Phu, N. H.; Rohlwink, U.; Thwaites, G. E. The neurocritical care of tuberculous meningitis. *Lancet Neurol.* **2019**, *18*, 771−783.

(6) Thwaites, G. E.; Toorn, R. V.; Schoeman, J. Tuberculous meningitis: more questions, still too few answers. *Lancet Neurol.* **2013**, *12*, 999−1010.

(7) Wilkinson, R. J.; Rohlwink, U.; Misra, U. K.; Crevel, R. V.; Mai, N. T. H.; Dooley, K. E.; Caws, M.; Figaji, A.; Savic, R.; Solomons, R.; Thwaites, G. E. Tuberculous meningitis. *Nat. Rev. Neurol.* **2017**, *13*, 581−598.

(8) van Laarhoven, A.; Dian, S.; Aguirre-Gamboa, R.; Avila-Pacheco, J.; Ricano-Ponce, I.; Ruesen, C.; Annisa, J.; Koeken, V.; Chaidir, L.; Li, Y.; Achmad, T. H.; Joosten, L. A. B.; Notebaart, R. A.; Ruslami, R.; Netea, M. G.; Verbeek, M. M.; Alisjahbana, B.; Kumar, V.; Clish, C. B.; Ganiem, A. R.; van Crevel, R. V. Cerebral tryptophan metabolism and outcome of tuberculous meningitis: an observational cohort study. *Lancet Infect. Dis.* **2018**, *18*, 526−535.

(9) Modoux, M.; Rolhion, N.; Mani, S.; Sokol, H. Tryptophan metabolism as a pharmacological target. *Trends Pharmacol. Sci.* **2021**, *42*, 60−73.

(10) Sonner, J. K.; Keil, M.; Falk-Paulsen, M.; Mishra, N.; Rehman, A.; Kramer, M.; Deumelandt, K.; Rowe, J.; Sanghvi, K.; Wolf, L.; Landenberg, A. V.; Wolff, H.; Bharti, R.; Oezen, I.; Lanz, T. V.; Wanke, F.; Tang, Y.; Brandao, I.; Mohapatra, S. R.; Epping, L.; Grill, A.; Roth, R.; Niesler, B.; Meuth, S. G.; Opitz, C. A.; Okun, J. G.; Reinhardt, C.; Kurschus, F. C.; Wick, W.; Bode, H. B.; Rosenstiel, P.; Platten, M. Dietary tryptophan links encephalogenicity of autoreactive T cells with gut microbial ecology. *Nat. Commun.* **2019**, *10*, No. 4877.

(11) Tomalka, J.; Sharma, A.; Smith, A. G. C.; Avaliani, T.; Gujabidze, M.; Bakuradze, T.; Sabanadze, S.; Jones, D. P.; Avaliani, Z.; Kipiani, M.; Kempker, R. R.; Collins, J. M. Combined cerebrospinal fluid metabolomic and cytokine profiling in tuberculosis

meningitis reveals robust and prolonged changes in immunometabolic networks. *Tuberculosis* **2024**, *144*, No. 102462.
(12) Li, Y. J.; Yang, L. L.; Ni, L.; Xiong, J. M.; He, J. Y.; Zhou, L. D.; Luo, L.; Zhang, Q. H.; Yuan, C. S. Constructing electrochemical sensor using molecular-imprinted polysaccharide for rapid identification and determination of l-tryptophan in diet. *Food Chem.* **2023**, *425*, No. 136486.
(13) Murugan, E.; Kumar, K. Fabrication of SnS/TiO_2@GO composite coated glassy carbon electrode for concomitant determination of paracetamol, tryptophan, and caffeine in pharmaceutical formulations. *Anal. Chem.* **2019**, *91*, 5667−5676.
(14) Rouxel, J. R.; Nam, Y.; Chernyak, V. Y.; Mukamel, S. Manipulating ultrafast even-order nonlinear chiral responses of L-tryptophan by polarization pulse shaping. *Proc. Natl. Acad. Sci. U.S.A.* **2024**, *121*, No. e2402660121.
(15) Jiang, W.; Lee, S.; Zan, G.; Zhao, K.; Park, C. Alternating current electroluminescence for human-interactive sensing displays. *Adv. Mater.* **2024**, *36*, No. e2304053.
(16) Li, J.; Wang, S. P.; Zong, G.; Kim, E.; Tsao, C. Y.; VanArsdale, E.; Wang, L. X.; Bentley, W. E.; Payne, G. F. Interactive materials for bidirectional redox-based communication. *Adv. Mater.* **2021**, *33*, No. e2007758.
(17) Li, Z.; Peng, W.; Zhou, J.; Shui, S.; Liu, Y.; Li, T.; Zhan, X.; Chen, Y.; Lan, F.; Ying, B.; Wu, Y. Multidimensional interactive cascading nanochips for detection of multiple liver diseases via precise metabolite profiling. *Adv. Mater.* **2024**, *36*, No. e2312799.
(18) Cai, W.; Wang, J.; Chu, C.; Chen, W.; Wu, C.; Liu, G. Metal-organic framework-based stimuli-responsive systems for drug delivery. *Adv. Sci.* **2019**, *6*, No. 1801526.
(19) Deshmukh, A. P.; Chen, Y. N.; Cleron, J. L.; Tie, M.; Wen, J. J.; Heinz, T. F.; Fiip, Ma R.; Karunadasa, H. I. Tuning the quantum-well structure of single-crystal layeredperovskite heterostructures. *J. Am. Chem. Soc.* **2025**, *147*, 40171−40181.
(20) Li, M.; Chen, L.; Teng, R. M.; Chen, Z. K.; Yan, Z. J.; Lv, X. Y.; Ding, C. P.; Huang, Y. J. Surface hot-electron transfer-driven site-specific growth of Pt nanoisland onto Au NR@CeO_2 dumbbells with exceptional H_2O_2 affinity for ultra-sensitive vitro diagnosis. *Adv. Funct. Mater.* **2025**, No. e17816.
(21) Ding, C. P.; Chen, W. W.; Teng, R. M.; Chen, Z. K.; Zhao, Y. B.; Sun, Y.; Lin, J. L.; Li, M.; Huang, Y. J. Nanocomposite indicator-based high-resolution naked-eye hue sensor for catecholamine detection. *Anal. Chem.* **2025**, *97*, 15253−15261.
(22) Teng, R. M.; Li, M.; Chen, Z. K.; Lin, J. L.; Zhang, Y. H.; Li, H.; Yan, Z. J.; Zhang, D. Y.; Ding, C. P.; Huang, Y. J. Intelligent screening of prostate cancer individuals using an enzyme-assisted multicolor visualization platform. *Adv. Sci.* **2025**, *12*, No. 2408825.
(23) Xue, C.; Li, G.; Zheng, Q.; Gu, X.; Shi, Q.; Su, Y.; Chu, Q.; Yuan, X.; Bao, Z.; Lu, J.; Li, L. Tryptophan metabolism in health and disease. *Cell Metab.* **2023**, *35*, 1304−1326.
(24) Li, L.; Luo, Y.; Jia, L. Genetically engineered bacterium-modified magnetic particles assisted chiral recognition and colorimetric determination of *D*/*L*-tryptophan in millets. *Food Chem.* **2023**, *407*, No. 135125.
(25) Shen, B. Y.; Chen, X.; Shen, K.; Xiong, H.; Wei, F. Imaging the node-linker coordination in the bulk and local structures of metal-organic frameworks. *Nat. Commun.* **2020**, *11*, No. 2692.
(26) Zhang, D. L.; Zhu, Y. H.; Liu, L. M.; Ying, X. G.; Hsiung, C. E.; Sougrat, R.; Li, K.; Han, Y. Atomic-resolution transmissionelectron microscopy of electronbeam-sensitive crystalline materials. *Science* **2018**, *359*, 675−679.
(27) Kagan, C. R.; Mitzi, D. B.; Dimitrakopoulos, C. D. Organic-inorganic hybrid materials as semiconducting channels in thin-film field-effect transistors. *Science* **1999**, *286*, 945−947.
(28) Wang, C.; He, Q.; Halim, U.; Liu, Y.; Zhu, E.; Lin, Z.; Xiao, H.; Duan, X.; Feng, Z.; Cheng, R.; Weiss, N. O.; Ye, G.; Huang, Y. C.; Wu, H.; Cheng, H. C.; Shakir, I.; Liao, L.; Chen, X.; Goddard, W. A.; Huang, Y.; Duan, X. Monolayer atomic crystal molecular superlattices. *Nature* **2018**, *555*, 231−236.
(29) Zhang, W.; Saliba, M.; Moore, D. T.; Pathak, S. K.; Horantner, M. T.; Stergiopoulos, T.; Stranks, S. D.; Eperon, G. E.; Alexander-Webber, J. A.; Abate, A.; Sadhanala, A.; Yao, S.; Chen, Y.; Friend, R. H.; Estroff, L. A.; Wiesner, U.; Snaith, H. J. Ultrasmooth organic-inorganic perovskite thin-film formation and crystallization for efficient planar heterojunction solar cells. *Nat. Commun.* **2015**, *6*, No. 6142.
(30) Zhao, B.; Wan, Z.; Liu, Y.; Xu, J.; Yang, X.; Shen, D.; Zhang, Z.; Guo, C.; Qian, Q.; Li, J.; Wu, R.; Lin, Z.; Yan, X.; Li, B.; Zhang, Z.; Ma, H.; Li, B.; Chen, X.; Qiao, Y.; Shakir, I.; Almutairi, Z.; Wei, F.; Zhang, Y.; Pan, X.; Huang, Y.; Ping, Y.; Duan, X.; Duan, X. High-order superlattices by rolling up van der Waals heterostructures. *Nature* **2021**, *591*, 385−390.
(31) Duan, H.; Yan, N.; Yu, R.; Chang, C. R.; Zhou, G.; Hu, H. S.; Rong, H.; Niu, Z.; Mao, J.; Asakura, H.; Tanaka, T.; Dyson, P. J.; Li, J.; Li, Y. Ultrathin rhodium nanosheets. *Nat. Commun.* **2014**, *5*, No. 3093.
(32) Gonzalez, D. H.; Kuang, X. M.; Scott, J. A.; Rocha, G. O.; Paulson, S. E. Terephthalate probe for hydroxyl radicals: yield of 2-hydroxyterephthalic acid and transition metal interference. *Anal. Lett.* **2018**, *51*, 2488−2497.
(33) żamojć, K.; Zdrowowicz, M.; Rudnicki-Velasquez, P. B.; Krzyminski, K.; Zaborowski, B.; Niedzialkowski, P.; Jacewicz, D.; Chmurzynski, L. The development of 1,3-diphenylisobenzofuran as a highly selective probe for the detection and quantitative determination of hydrogen peroxide. *Free Radical Res.* **2017**, *51*, 38−46.
(34) Zhao, H.; Zhang, R.; Yan, X.; Fan, K. Superoxide dismutase nanozymes: an emerging star for anti-oxidation. *J. Mater. Chem. B* **2021**, *9*, 6939−6957.
(35) Gale, C. B.; Yan, Z. B.; Fefer, M.; Goward, G. R.; Brook, M. A. Synthesis of siliconized photosensitizers for use in $^1O_2$-generating silicone elastomers: an electron paramagnetic resonance study. *Macromolecules* **2021**, *54*, 4333−4341.
(36) Suzen, S.; Gurer-Orhan, H.; Saso, L. Detection of reactive oxygen and nitrogen species by electron paramagnetic resonance (EPR) technique. *Molecules* **2017**, *22*, No. 181.
(37) Shi, Y.; Schimmenti, R.; Zhu, S.; Venkatraman, K.; Chen, R.; Chi, M.; Shao, M.; Mavrikakis, M.; Xia, Y. Solution-phase synthesis of PdH(0.706) nanocubes with enhanced stability and activity toward formic acid oxidation. *J. Am. Chem. Soc.* **2022**, *144*, 2556−2568.
(38) Sun, G.; Zhao, Z. J.; Mu, R.; Zha, S.; Li, L.; Chen, S.; Zang, K.; Luo, J.; Li, Z.; Purdy, S. C.; Kropf, A. J.; Miller, J. T.; Zeng, L.; Gong, J. Breaking the scaling relationship via thermally stable Pt/Cu single atom alloys for catalytic dehydrogenation. *Nat. Commun.* **2018**, *9*, No. 4454.
(39) Yan, Q. Q.; Wu, D. X.; Chu, S. Q.; Chen, Z. Q.; Lin, Y.; Chen, M. X.; Zhang, J.; Wu, X. J.; Liang, H. W. Reversing the charge transfer between platinum and sulfur-doped carbon support for electrocatalytic hydrogen evolution. *Nat. Commun.* **2019**, *10*, No. 4977.

https://doi.org/10.1021/acsnano.5c21167
ACS Nano 2026, 20, 5238−5249